



Iron nuclearity in mineral fibres: Unravelling the catalytic activity for predictive modelling of toxicity

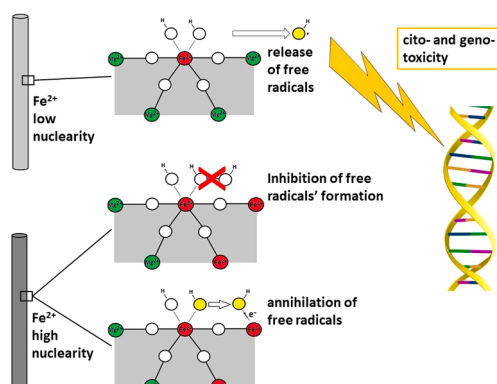
Alessandro F. Gualtieri^{*}, Marina Cocchi, Francesco Muniz-Miranda, Alfonso Pedone, Elena Castellini, Lorenzo Strani

Chemical and Geological Sciences Department, 41125, University of Modena and Reggio Emilia, Modena, Italy

HIGHLIGHTS

- Iron nuclearity of mineral fibres has been assessed from the analysis of UV-Vis spectra.
- Mineral fibres display very different iron nuclearity depending on their structure model.
- A model explaining the catalytic activity of iron is proposed.
- Fibres containing isolated Fe^{2+} have higher capacity for producing toxic free radicals.
- Iron nuclearity supports the FPTI quantitative model for predicting the toxicity of mineral fibres.

GRAPHICAL ABSTRACT



ARTICLE INFO

Keywords:

Mineral fibres
Iron nuclearity
UV-Vis spectroscopy
ab initio calculations
Multivariate curve resolution

ABSTRACT

Chronic inflammation induced in vivo by mineral fibres, such as asbestos, is sustained by the cyclic formation of cytotoxic/genotoxic oxidant species that are catalysed by iron. High catalytic activity is observed when iron atoms are isolated in the crystal lattice (nuclearity=1), whereas the catalytic activity is expected to be reduced or null when iron forms clusters of higher nuclearity.

This study presents a novel approach for systematically measuring iron nuclearity across a large range of iron-containing standards and mineral fibres of social and economic importance, and for quantitatively assessing the relation between nuclearity and toxicity. The multivariate curve resolution (MCR) empirical approach and density functional theory (DFT) calculations were applied to the analysis of UV-Vis spectra to obtain information on the nature of iron and nuclearity.

This approach led to the determination of the nuclearity of selected mineral fibres which was subsequently used to calculate a toxicity-related index. High nuclearity-related toxicity was estimated for chrysotile samples, fibrous glaucophane, asbestos tremolite, and fibrous wollastonite. Intermediate values of toxicity, corresponding to a mean nuclearity of 2, were assigned to actinolite asbestos, amosite, and crocidolite. Finally, a low nuclearity-related toxicity parameter, corresponding to an iron-cluster with a lower catalytic power to produce oxidants, was assigned to asbestos anthophyllite.

^{*} Corresponding author.

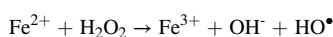
E-mail address: alessandro.gualtieri@unimore.it (A.F. Gualtieri).

1. Introduction

The catalytic properties of a material can affect its toxicity. Low catalytic toxicity can affect small microorganisms such as bacteria [2,3], medium toxicity can affect abnormal cells [41], and high toxicity can affect animals [4] and humans [51].

Iron is the most studied transition metal and its catalytic properties and toxicity *in vitro/in vivo* are dependent upon its nuclearity [26]. According to the IUPAC [32] definition, nuclearity is the number of central atoms (iron in this case) joined in a single coordination entity by bridging ligands or metal-metal bonds. Hence, iron nuclearity can be monomeric (single iron atom, no other iron atoms in the second shell), dimeric (a cluster of two iron atoms, connected by one bridging oxygen atom), trimeric (a cluster of three iron atoms, connected by several bridging oxygen atoms), etc. [69].

Studies on the iron chemical environment in zeolite species have highlighted isolated $(\text{FeO})^{2+}$ monomeric structures as the preferred catalytic active sites. They thus serve as primary sites for the production of cyto-/geno-toxic oxidant species such as the hydroxyl radical HO^\bullet via the Fenton reaction [30,38]:



Paired Fe-O-Fe active species or Fe_xO_y clusters and clustered iron with high nuclearity should exhibit reduced activity or be inactive [26].

Gualtieri [24,25] showed that iron nuclearity plays a role in the quantitative model proposed for the assessment of the toxicity/pathogenicity potential of mineral fibres. This model is based on the Fibre Potential Toxicity/Pathogenicity Index (FPTI) which takes into account all the fibre parameters that induce the biological mechanisms responsible for adverse *in vitro* and *in vivo* effects: morphometric (the fibre length, width, crystal curvature, crystal habit, density, hydrophobic character of the surface, surface area); chemical (total iron content, ferrous iron, surface ferrous iron/iron nuclearity, content of metals other than iron); biodurability-related (dissolution rate, velocity of iron release, velocity of silica dissolution, velocity of metal release); and surface activity (zeta potential, fibre aggregation, cation exchange).

Iron nuclearity requires an in-depth analysis because now it is arbitrarily defined in the FPTI model as: (i) if iron (namely Fe^{2+}) displays high nuclearity (> 2), it is assumed that the catalytic activity for producing HO^\bullet is low and hence a low toxicity index of 0.02 is assigned; (ii) if iron displays nuclearity = 2 (dimeric), it is assumed that the catalytic activity to produce HO^\bullet is moderate and hence a low toxicity index of 0.03 is assigned; (iii) if iron is isolated (nuclearity = 1, monomeric), it is assumed that the catalytic activity for producing HO^\bullet is high and hence a high toxicity index of 0.07 is assigned. Understanding and quantitatively determining iron nuclearity is thus of paramount importance in order to rigorously define its role, reveal possible correlations with other iron-related parameters (the total iron content and ferrous iron content), and improve the model for the assessment of the toxicity/carcinogenicity potential of mineral fibres.

The precise definition of iron nuclearity and the related catalytic/toxicity properties of mineral fibres is very problematic. In general, analysing the iron chemical environment in minerals is challenging due to the diverse and complex nature of natural materials. Iron can exist in multiple oxidation states, and its interaction with various ligands and mineral matrices makes it difficult to characterize its chemical environment. The presence of impurities, substitutions in the crystal lattice and structure defectivity further complicate the analysis. The heterogeneity of natural mineral samples thus makes it challenging to obtain representative data, and often the concentration of catalytically active iron is close to or below the detection limits of the experimental methods.

Besides the nature of the investigated materials, the paramagnetic properties of iron pose challenges for certain spectroscopic techniques. Traditional methods, such as X-ray diffraction, may provide valuable

information on the mineral structure, but often fall short of offering detailed insights into the iron's chemical speciation. Advanced spectroscopic techniques such as Mössbauer spectroscopy and X-ray absorption spectroscopy (XANES, EXAFS) have been employed, however they are not routine analytical methods and their application requires sophisticated instruments and access to synchrotron facilities. For all these reasons, the lack of a robust body of experimental data on the iron chemical environment in mineral fibres has prevented its accurate measurement and parametrization. Among the noteworthy case studies within the literature, our current understanding, as authors, is primarily informed by the following:

- (1) Martra et al. [45] exploited infrared spectroscopy of NO probe and UV-Vis-NIR spectroscopy to determine reactive iron sites at the surface of crocidolite capable of producing free radicals. This infrared method is based on the use of NO as a titrant of the exposed (sub-surface) sites and exploits the affinity of NO towards Fe^{2+} and Fe^{3+} centres, leading to the formation of $\text{Fe}^{x+}(\text{NO})_n$ nitrosyls characterized by intense $\nu(\text{NO})$ bands [69]. Martra et al. [45] managed to assign dimeric (dinitrosyl species stabilized on highly coordinated unsaturated Fe^{2+} ions) and monomeric (mononitrosyl adducts on highly coordinated unsaturated Fe^{2+} centres) iron species, although problems of interpretation arose due to the weak signals of the spectra. This method has a sensitivity problem and cannot be applied to natural systems with a low iron content.
- (2) Schwidder et al. [61] used UV-Vis diffuse reflectance spectroscopy to analyse the iron site structure in synthetic Fe-ZSM-5 with a low (< 1.2 wt% Fe) iron content. The authors assigned the bands at ~ 220 nm and ~ 285 nm to $\text{Fe}^{3+} \leftarrow \text{O}$ charge transfer bands of isolated iron ions in tetrahedral and octahedral coordination, respectively ($t_1 \rightarrow t_2/t_1 \rightarrow e$ transitions unresolved). The band at ~ 350 nm and sub-bands above 400 nm were also assigned to oligomeric clusters and large particles, respectively.
- (3) Pirngruber et al. [54] used UV-Vis spectroscopy to determine the nuclearity of iron sites in synthetic Fe-ZSM-5 with a low concentration ($< 1\%$ Fe). Fe^{3+} cations were assigned to an isolated octahedral environment, however, the authors expressed doubts regarding the assignment and interpretation of the UV-Vis data.
- (4) Zecchina et al. [69] studied exposed Fe^{x+} species in synthetic Fe-silicalites with IR spectroscopy of NO moiety. Similar to case (1), this method encountered sensitivity issues, particularly when dealing with low iron concentrations.
- (5) Zecchina et al. [69] also investigated the structure of Fe^{x+} species and $\text{Fe}^{2+}(\text{NO})_n$ complexes in Fe-ZSM-5 and Fe-silicalite using UV-Vis NIR spectroscopy. However, the UV-Vis spectra of NO adsorbed-on Fe-silicalite activated in vacuum at 773 K they lacked a detailed assignment of the UV-Vis bands in terms of mono-, di- and tri-nitrosyl.
- (6) Borghi et al. [8] investigated iron-doped synthetic chrysotiles using UV-Vis diffuse reflectance spectroscopy and EPR and identified: (i) two isolated Fe^{3+} sites, in tetrahedral and octahedral coordination; and (ii) exchange-coupled Fe^{3+} paramagnetic ions in Fe_xO_y clusters.

The promising results obtained with UV-Vis spectroscopy on mineral fibres [45,8] prompted us to systematically investigate a suite of iron-containing synthetic and natural standards, including mineral fibres, with UV-Vis spectroscopy to gain insights into both the oxidation state and nuclearity. Our research includes three complementary research lines of inquiry:

- (i) We conducted *ab initio* calculations employing density functional theory (DFT) to interpret UV-Vis spectra of iron atoms with different nuclearity and oxidation states in different crystalline matrices using a cluster approach, as detailed in Section 2.4. We

Table 1

Natural and synthetic iron-containing samples used as standards with known iron oxidation states and chemical environments.

sample	Origin	sample purity	chemical formula	iron oxidation state	iron chemical environment	Iron mass (%)
ammonium iron oxalate trihydrate	Synthetic, Merck	yes	$(\text{NH}_4)_3[\text{Fe}(\text{C}_2\text{O}_4)_3] \cdot 3 \text{H}_2\text{O}$	Fe^{3+}	isolated	13.0
ammonium iron sulphate dodecahydrate	Synthetic, Merck	yes	$(\text{NH}_4)_2\text{Fe}(\text{SO}_4)_2 \cdot 12 \text{H}_2\text{O}$	Fe^{2+}	isolated	11.6
goethite	Synthetic, Bayer	yes	FeOOH	Fe^{3+}	Cluster (6 iron atoms in the second shell)	62.9
hematite	Natural, Elba island (Italy)	yes	Fe_2O_3	Fe^{3+}	Cluster (6 iron atoms in the second shell)	69.9
iron chloride	Synthetic, Merck	yes	FeCl_3	Fe^{3+}	Cluster (4 iron atoms in the second shell)	34.4
iron phosphate dihydrate	Synthetic, Merck	yes	$\text{FePO}_4 \cdot 2 \text{H}_2\text{O}$	Fe^{3+}	isolated	27.9
iron sulphate hydrate	Synthetic, Merck	yes	$\text{Fe}_2(\text{SO}_4)_3 \cdot \text{H}_2\text{O}$	Fe^{3+}	isolated	26.7
iron sulphate heptahydrate	Synthetic, Merck	yes	$\text{FeSO}_4 \cdot 7 \text{H}_2\text{O}$	Fe^{2+}	isolated	7.5
magnetite	Natural, Cogne, Aosta Valley (Italy)	yes	Fe_3O_4	$\text{Fe}^{2+}, \text{Fe}^{3+}$	Cluster (6 iron atoms in the second shell)	72.4
iron	Natural, GEMMA 1786 museum mineral collection, Modena (Italy)	yes	Fe	Fe	Cluster (6 iron atoms in the second shell)	100.0
kaolinite	Natural, Washington County, Georgia (USA)	yes	$\text{Al}_{3.66}\text{Fe}_{0.07}\text{Ti}_{0.16}(\text{OH})_8\text{Si}_4\text{O}_{10}$	Fe^{3+}	isolated	0.05
olivine	Natural, Balmuccia, Vercelli (Italy)	yes	$\text{Mg}_{1.845}\text{Fe}_{0.155}\text{SiO}_4$	Fe^{2+}	dimeric or trimeric	12.3
olivine calcined 1200 °C in air	Natural, Balmuccia, Vercelli (Italy)	Yes, hematite formed	$\text{Mg}_{1.845}\text{Fe}_{0.155}\text{SiO}_4$	Fe^{3+}	Cluster (6 iron atoms in the second shell)	12.3
pyrope (iron-containing garnet)	Natural, Piedmont, Italy	yes	$\text{Mg}_{2.79}\text{Fe}_{0.15}\text{Ca}_{0.04}\text{Al}_{2.02}\text{Si}_{2.99}\text{O}_{12}$	Fe^{2+}	Isolated (possibly dimeric?)	6.7
pyroxene (iron-containing diopside)	Natural, GEMMA 1786 museum mineral collection, Modena (Italy)	yes	$\text{Ca}(\text{Mg},\text{Fe})\text{Si}_2\text{O}_6$	Fe^{2+}	Isolated (possibly dimeric?)	1.0?
siderite	Natural, Fabriano, Marche (Italy)	yes	FeCO_3	Fe^{2+}	Cluster (6 iron atoms in the second shell)	48.2
talc	Borgotaro (Parma, Italy)	yes	$\text{Mg}_{2.65}\text{Al}_{0.01}\text{Fe}_{0.12}(\text{OH})_2\text{Si}_{4.04}\text{O}_{10}$	Fe^{3+}	Cluster	< 0.1

also used studies of FTIR/RAMAN spectra of amorphous iron-rich systems (see for example, [64]);

- (ii) We examined the parameters extracted from the UV-Vis spectra of the samples in search of trends dependent on the iron oxidation state and nuclearity (see for example [37]);
- (iii) We employed a spectral unmixing method, namely multivariate curve resolution (MCR), to the UV-Vis spectra in order to develop characteristic profiles of each iron form and to obtain a relative concentration matrix for use in evaluating the state of iron in the mineral fibres studied.

There are four main reasons why we selected a bulk technique such as UV-Vis spectroscopy over surface-sensitive experimental methods: (1) the high sensitivity of this bulk method in detecting iron in solid matrices has been demonstrated in previous studies (see for example iron in carbon nanotubes in [1]); (2) surface characteristics of specimens can be contingent upon environmental conditions (sample preparation, measurement of cell atmosphere, humidity) thereby introducing unpredictable variability in surface measurements; (3) bulk measurements are preferred over surface measurements for the FPTI model, which aims to classify the potential toxicity/pathogenicity of a mineral fibre. This preference is rooted in the need to prevent bias arising from sample impurities which are almost invariably present at the fibre surface; (4) the dissolution of mineral fibres *in vitro/in vivo* generally follows a contracting volume kinetic model [27], and, as the dissolution reaction proceeds, the original bulk of the fibre is transformed into the new surface of the fibre.

In this work, for what we believe is the first time, we attempt to classify mineral fibres of social and economic importance based on their iron nuclearity which in turn affects the potential toxicity of the fibres.

UV-Vis spectroscopy was used to obtain information on the chemical environment of iron. First, *ab initio* DFT modelling of selected ideal standards with known chemical environments was used to produce simulated patterns and to verify whether the shape of the UV-Vis spectra changes with the iron chemical environment of the sample. The next

step was the qualitative analysis of the UV-Vis spectra to assess whether the relationships hold for real samples of iron-containing standards and mineral fibres. MCR was then used to quantitatively assess this dependence and classify the mineral fibres in terms of iron nuclearity. The features of the spectra of all the standards were plotted to search for clusters with different iron chemical environments. In this way, it is possible to predict the iron nuclearity of a sample from the signature of the UV-Vis spectrum. This information is then used to calculate the iron nuclearity-related toxicity parameter in the FPTI model to predict the toxicity/carcinogenicity of mineral fibres.

2. Materials and methods

2.1. Theoretical background

This work is based on the assumption that iron nuclearity, which influences the toxicity/pathogenicity potential of the carrier material, shapes the profile of its UV-Vis spectrum. In the general case of iron, there are three types of electronic transitions in the optical spectra of Fe^{3+} -containing minerals [63]:

- Fe^{3+} ligand field transitions. The $\text{Fe}(3d)$ atomic orbitals in octahedral coordination are split into two sets of orbitals labelled t_{2g} and e_g , and the orbital energy separation is ruled by the crystal field splitting. In the case of an isolated iron atom (monomeric), all of the transitions from the ground state to the excited ligand field states are, in principle, both spin and parity-forbidden. However, these transitions are permitted through the magnetic coupling of the electronic spins of the next-nearest neighbour iron atoms [44] as in dimeric, trimeric ... assemblages.
- Ligand-to-metal charge-transfer transitions (LMCT), at energies higher than most of the ligand field transitions, are described by the molecular orbital theory [63]. This is ideally a monomeric case.
- Transitions resulting from the simultaneous excitation of magnetically-coupled Fe^{3+} cations (as in dimeric/trimeric/...

assemblages) which occupy adjacent sites. The magnetic coupling generates new absorption features corresponding to the simultaneous excitation of two iron centres (Schugar et al., 1972) in double exciton processes with spin-allowed transitions.

According to Sherman and Waite [63], in the case of iron-oxides/hydroxides (composed of Fe_xO_y cluster of iron atoms), absorption bands near 430, 360–380, and 290–310 nm correspond to ligand field transitions of Fe^{3+} (possible because of the magnetic coupling). At wavelengths below 270 nm, absorption bands are assigned to LMCT transitions, whereas the bands in the region 485–550 nm are assigned to the excitation of an iron-iron pair (“double exciton processes”).

Pirngruber et al. [54] confirmed that UV-Vis spectra contain information on the electronic structure and symmetry of metal ions and that intense bands at lower energies indicate iron clusters of higher nuclearity. Hence, UV-Vis absorption bands can be classified into three categories, yielding a qualitative indication of the nuclearity of the iron species [49,53,54]: (i) isolated species absorbing at wavelength < 300 nm; (ii) small oligonuclear Fe_xO_y clusters absorbing between 300 and 400 nm; (iii) Fe_2O_3 nanoparticles absorbing at wavelength > 400 nm.

In agreement with this, Borghi et al. [8] observed that in Fe^{3+} -doped synthetic chrysotile, the $d-d$ transitions, which are forbidden for both spin and Laporte selection rules, are permitted or assisted through the magnetic coupling of electronic spins of next-nearest neighbour Fe^{3+} cations. These authors also reported that LMCT bands for the isolated $[\text{FeO}_4]$ tetrahedral group were observed in the 215–240 nm range, and bands between 270–290 nm were detected for isolated octahedral $[\text{FeO}_6]$ group, while due to octahedral Fe^{3+} in cluster-like Fe_xO_y species, LMCT bands were found between 300 and 400 nm.

2.2. Standard materials and samples: characterization and iron chemical environment

Table 1 reports the list of iron-containing samples used as standards in this study. For each sample, iron oxidation state and nuclearity were estimated a priori. Table 1 includes the origin of the samples, the chemical formula, the information on the structure of the iron site and its content.

Besides the standard samples, a selection of relevant mineral fibres were collected in order to predict the iron chemical environment and nuclearity: actinolite asbestos from Aurina Valley, Bolzano (Italy) with the following chemical formula $\text{K}_{0.02}\text{Na}_{0.05}(\text{Na}_{0.08}\text{Ca}_{1.92})_{\Sigma=2.00}(\text{Mg}_{3.80}\text{Fe}_{0.79}\text{Fe}_{0.11}\text{Al}_{0.20}\text{Mn}_{0.05}\text{Ni}_{0.02}\text{Cr}_{0.01})_{\Sigma=4.98}(\text{Si}_{7.67}\text{Al}_{0.25})_{\Sigma=7.92}\text{O}_{21.69}(\text{OH})_{2.31}$ [58]; amosite from Penge mine, Northern Province (South Africa): $(\text{Ca}_{0.02}\text{Na}_{0.01})(\text{Fe}_{5.36}^{2+}\text{Mg}_{1.48}\text{Fe}_{0.11}\text{Mn}_{0.06})_{\Sigma=7.01}(\text{Si}_{7.93}\text{Al}_{0.01})_{\Sigma=7.94}\text{O}_{21.94}(\text{OH})_{2.06}$ [55]; UICC standard anthophyllite asbestos (Finnish NB #4173–111-5) from Paakkila (Finland): $\text{Ca}_{0.04}(\text{Mg}_{5.81}\text{Fe}_{0.92}^{2+}\text{Fe}_{0.21}^{3+}\text{Mn}_{0.04})_{\Sigma=6.98}(\text{Si}_{7.83}\text{Al}_{0.02})_{\Sigma=7.85}\text{O}_{21.63}(\text{OH})_{2.37}$ [60]; chrysotile from Balangero mine (Turin, Italy): $(\text{Mg}_{5.81}\text{Fe}^{2+}_{0.15}\text{Al}_{0.27}\text{Fe}_{0.09}^{3+}\text{Cr}_{0.01})\text{Si}_{3.97}\text{O}_{10}(\text{OH})_{7.11}$ [59]; commercial chrysotile from Yasnii mine, Orenburg Minerals (Russia): $(\text{Mg}_{5.739}\text{Fe}_{0.054}^{2+}\text{Fe}_{0.089}^{3+}\text{Al}_{0.068}\text{Cr}_{0.010}\text{Ni}_{0.011}\text{Si}_{3.964}\text{O}_{10}\text{OH}_8$ [12]; the UICC standard crocidolite South African NB #4173–111-3: $(\text{Na}_{1.96}\text{Ca}_{0.03}\text{K}_{0.01})_{\Sigma=2}(\text{Fe}_{2.54}^{2+}\text{Fe}_{0.25}^{3+}\text{Mg}_{0.52})_{\Sigma=4.91}(\text{Si}_{7.84}\text{Al}_{0.02})_{\Sigma=7.86}\text{O}_{21.36}(\text{OH})_{2.64}$ [55]; fibrous glaucophane from San Anselmo, Marin County (CA, USA): $(\text{Na}_{1.61}\text{Ca}_{0.43}\text{K}_{0.01})_{\Sigma=2.04}(\text{Fe}_{1.31}^{2+}\text{Fe}_{0.70}^{3+}\text{Mg}_{2.01}\text{Al}_{1.00}\text{Mn}_{0.06})_{\Sigma=5.08}\text{Si}_{8.09}\text{O}_{22}(\text{OH})_2$ [14]; tremolite asbestos from the Ultrabasic Lanzo Massif in the Occidental Alps (Lanzo Valley, Piedmont): $(\text{Ca}_{1.91}\text{Na}_{0.06}\text{K}_{0.01})_{\Sigma=1.98}(\text{Mg}_{4.71}\text{Fe}_{0.22}^{2+}\text{Fe}_{0.08}^{3+}\text{Mn}_{0.02})_{\Sigma=5.03}(\text{Si}_{8.01}\text{Al}_{0.02})_{\Sigma=8.03}\text{O}_{22.14}(\text{OH})_{1.86}$ [55]; and commercial fibrous wollastonite NYAD G from Willsboro-Lewis (New York, USA): $\text{Ca}_{0.997}\text{Fe}_{0.005}^{2+}\text{Fe}_{0.002}^{3+}\text{Mn}_{0.003}\text{Si}_{0.979}\text{O}_3$ [13].

Each sample was ground in agate mortar, or with cryo-milling when necessary, using a Retsch mixer mill MM 400 (Düsseldorf, Germany).

The powders obtained were used for the UV-Vis experiments.

2.3. DR-UV-Vis spectroscopy

Diffuse reflectance (DR) UV-Vis spectra were acquired in the 200–800 nm range, using a UV-VIS-NIR (JASCO V-570) spectrophotometer equipped with an integrating sphere attachment (JASCO model ISN-470) to analyse the powder samples. BaSO_4 was used as a reference. The bandwidth was set at 10 nm, and the scan speed was 400 nm/min. For each measurement, 100 mg of the sample were used, ground as homogeneously as possible.

2.4. Ab initio calculations of selected standards

Ab initio calculations are state-of-the-art methods to predict the molecular and materials structure and properties which can be related to the activity of various harmful cells, bacteria, and hazardous chemicals such as inflammatory substances, exploiting quantitative structure-activity relationships models. For example, Alimirzai and Kieslich [5] developed a machine learning-based model to quantitatively predict anticancer activities before the experimental chemical design, which was subsequently applied to antiviral peptides [36].

In our study, because the focus is on the chemical state of iron to indirectly predict its toxicity potential, quantum chemistry calculations were employed. These calculations were used as the basis to interpret the electronic (UV-Vis) absorption spectra of selected standard minerals with the specific chemical environments of iron. Basically, with all the obvious limitations imposed by the fact that the models are created from simplified ideal structures, these calculations are intended to quantitatively confirm whether the position and intensity of the absorption bands depend on the chemical environment of iron.

Ab initio calculations were also conducted to investigate H_2O_2 splitting on silicate models with different levels of iron nuclearity.

For the simulation of UV-Vis spectra, we used time-dependent density Functional calculations (TDDFT) using Gaussian 16 [19]. We adopted non-periodic models (i.e. clusters) extracted from experimental crystal structures. The Becke-three parameter exchange functional (B3) in conjunction with the Lee-Parr-Yang correlation functional (LYP) [39, 7] were used. The investigated standards with the distinctive iron chemical environment are iron phosphate dihydrate with isolated Fe^{3+} atoms; iron sulphate with isolated Fe^{2+} atoms; goethite ($\text{Fe}^{3+}\text{O}(\text{OH})$) with a cluster of six iron atoms in the second shell; siderite ($\text{Fe}^{2+}\text{CO}_3$) with a cluster of six iron atoms in the second shell and carbon-bonded oxygen atoms in the first shell. Details on the models are reported in Supplementary Information 1.

Each model contains two iron cations, along with the surrounding anions and/or molecules. As iron is present in all the minerals studied here, the combined electron-core potential and valence basis-set LANL2DZ was used, which has been extensively validated for transition metal atoms [16,48,47,67].

To explore the effect of Fe^{2+} nuclearity on H_2O_2 splitting, we used periodic DFT calculations on slab models of the most stable (010) face of the forsterite mineral (Mg_2SiO_4) [11]. The (010) face of forsterite has been taken as a prototype for possible facets in mineral fibres. It is also an ideal matrix to test iron nuclearity because forsterite is the magnesium end-member of the olivine mineral ($\text{Mg},\text{Fe}^{2+})_2\text{SiO}_4$), a solid solution with Fe^{2+} replacing Mg^{2+} in the octahedral cavities. The models built and used are reported in Supplementary Information 2. We generated a slab of 3 SiO_4 units with a 1×2 supercell (area of $5.992 \times 9.524 \text{ \AA}^2$) by cleaving from the bulk unit cell. The slab terminates with Mg^{2+} ions. Starting with this slab, we generated other two models by substituting 1 and 2 Mg^{2+} ions with Fe^{2+} . All the models were optimized using the PBE functional [52] using Norm-Conserving Pseudopotentials with a kinetic energy of 900 eV and a Monkhorst-Pack grid $2 \times 1 \times 1$. The CASTEP code was used for these calculations [62]. To correctly describe the localized behaviour of the iron 3d-orbital and reduce the

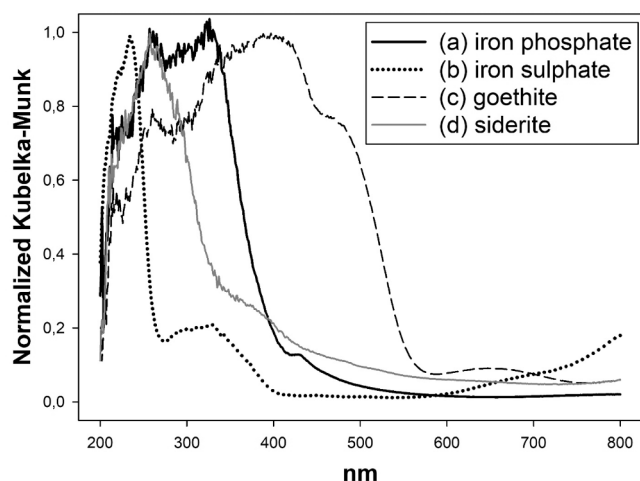


Fig. 1. The DR-UV-Vis spectra, in the 200–800 nm region, of selected standards with distinctive iron chemical environment. Legend: (a) iron phosphate dihydrate with isolated Fe^{3+} atoms; (b) iron sulphate with isolated Fe^{2+} atoms; (c) goethite ($\text{Fe}^{3+}\text{O}(\text{OH})$) with a cluster of 6 iron atoms in the second shell; (d) siderite ($\text{Fe}^{2+}\text{CO}_3$) with a cluster of 6 iron atoms in the second shell and carbon-bonded oxygen atoms in the first shell.

Self Interaction Error, we used a Hubbard parameter of 4.0 eV on 3d orbitals of iron [42]. Lastly, on the optimized models, we studied the adsorption mode and the thermodynamics of H_2O_2 splitting.

2.5. Preliminary analysis of the UV-Vis spectra

Exploratory analysis of parameters extracted from UV-Vis spectra was performed to qualitatively assess whether correlations or clustering trends could be identified with respect to the iron oxidation state and nuclearity, and to provide indications for subsequent quantitative analyses. Various parameters were thus calculated from the raw, normalized, and first derivative UV-Vis data, and respective scatter plots were examined.

The following parameters were tested: mean Kubelka-Munk (KM) value in the 200–800 nm range of the raw, normalized, and first derivative data; the wavelength corresponding to the maximum of the most intense absorption band located in the 200–800 nm range of the raw, normalized and first derivative data; and the position (nm) of the inflection point of the absorption band in the 200–800 nm range of the raw and normalized data. In addition, the iron mass percentage of the samples was also considered.

2.6. Multivariate Curve Resolution (MCR) to resolve the profile from UV-Vis spectra

Multivariate Curve Resolution – Alternating Least Squares (MCR-ALS) [10,34] is a well-established method for spectral unmixing aimed at recovering the spectral profiles of single components (pure constituents) in complex unresolved/unknown mixtures. MCR is a decomposition method that can extract pure contributions from overlapping signals. This approach is very useful for the analysis of spectroscopic data generated by complex matrices, as in our case, where the spectra collected consist of the UV-Vis absorbance contributions of multiple mineral fibres in each analysed sample. In fact, its ability to deal with overlapping spectral bands, namely their deconvolution, makes it suitable for the extraction of information related to the distinction among different nuclearity contributions.

Unlike principal component analysis (PCA) decomposition, MCR-ALS assumes that the data (**D**) follow a Lambert-Beer model (**D** is seen as a mixture of pure signals in different ratios): $\mathbf{D} = \mathbf{CS}^T + \mathbf{E}$. In the decomposition, **S** is a matrix that contains the pure contributions (i.e. the

resolved spectra), while **C** holds the concentrations (their “mixing ratios”), and **E** holds the part of **D** that is not modelled. Thus, MCR can also result in an efficient filtering method since undesired sources of variability – such as noise or background effects – can be efficiently removed, either ending up in the residual matrix **E**, or being explicitly modelled in specific components that describe baseline variations, etc.

Unlike curve fitting methodologies, pure spectral profiles do not need to be known a priori. The ALS algorithm is started by initially guessing either the **S** (selected in this work) or the **C** matrix, which can be random, but is usually estimated by the SIMPLISMA method [68], as in the present work. However, the MCR-ALS solution is not unique (rotational ambiguity), unless constraints are defined. These can be set based on the data/process studied. In this case, non-negativity in **C** and **S** profiles is imposed. The choice of the number of components is based on inspection of a plot (eigenvalues vs. component number) from a preliminary PCA model and on matching resolved profiles with reference ones from the analysed standards. MCR-ALS was applied on the KM-corrected spectra, as the absolute intensity may vary with instrumental sessions. Using MCR-ALS for feature extraction (i.e. relative concentration of the different resolved phases) overcomes the challenge of interpreting complex spectra. This is because the resulting pure profiles are more easily interpretable.

To assess the model’s performance, the concentration values for a test set (mineral fibres whose UV-Vis spectra were subsequently acquired) were predicted by inverting the MCR decomposition equation.

The MCR analysis was conducted using the freeware MCR MATLAB GUI v. 2.0 [34].

3. Results and discussion

To determine iron nuclearity, we systematically collected the UV-Vis spectra of standards with known nuclearity (see Fig. 1), interpreted them using DFT calculations in order to correlate the shape and features of the pattern to the iron oxidation number and nuclearity and developed a multivariate curve resolution (MCR) model. We thus obtained a pure spectral profile of each iron structure and their relative concentrations in the samples (which are the MCR features extracted from the spectra). This model was subsequently applied to obtain information on the iron nuclearity of mineral fibres with known toxicity and carcinogenicity potential, but with little information on the iron nuclearity.

3.1. Ab initio calculations of selected standards

As shown in Fig. 2, TD-DFT calculations enable a qualitative recovery of the spectral shape and profile of selected compounds, often with a blue shift of about 30–50 nm. Overall, the theoretical calculations suggest that minerals with more isolated Fe^{3+} cations adsorb at higher energies, as indicated by the spectrum of Fe^{3+} -phosphate (Fig. 2a). In contrast, in goethite (Fig. 2d), which is more akin to an Fe^{3+} cluster, we observe an increase in absorption bands even at long wavelengths. In the case of goethite, no frequency/wavelength shift seems necessary, but it should be highlighted that this model differs from all the others (Fe^{3+} -phosphate, Fe^{2+} -sulphate, and siderite) as it is in a low-spin state, because it better reproduces the relevant spectral features. The most important transitions, with the model employed here, seem to involve a larger charge transfer in the case of the high-spin Fe^{3+} compound compared to Fe^{2+} compounds. This is mostly due to a reduced inter-electronic repulsion for high-spin Fe^{2+} compared to high-spin Fe^{3+} . However, in the case of low-spin goethite Fe^{3+} , the most important electronic transitions involve a lower charge transfer as in the case of high-spin Fe^{2+} minerals. Fe^{2+} compounds (Fig. 2b and c) have an electronic spectrum peak in the 200–250 nm wavelength range, however, siderite (Fig. 2c) exhibits a particular behaviour with significant absorption bands also at low energy.

The ab initio calculations confirm the literature data and our data regarding a different distribution and shape of the bands originating

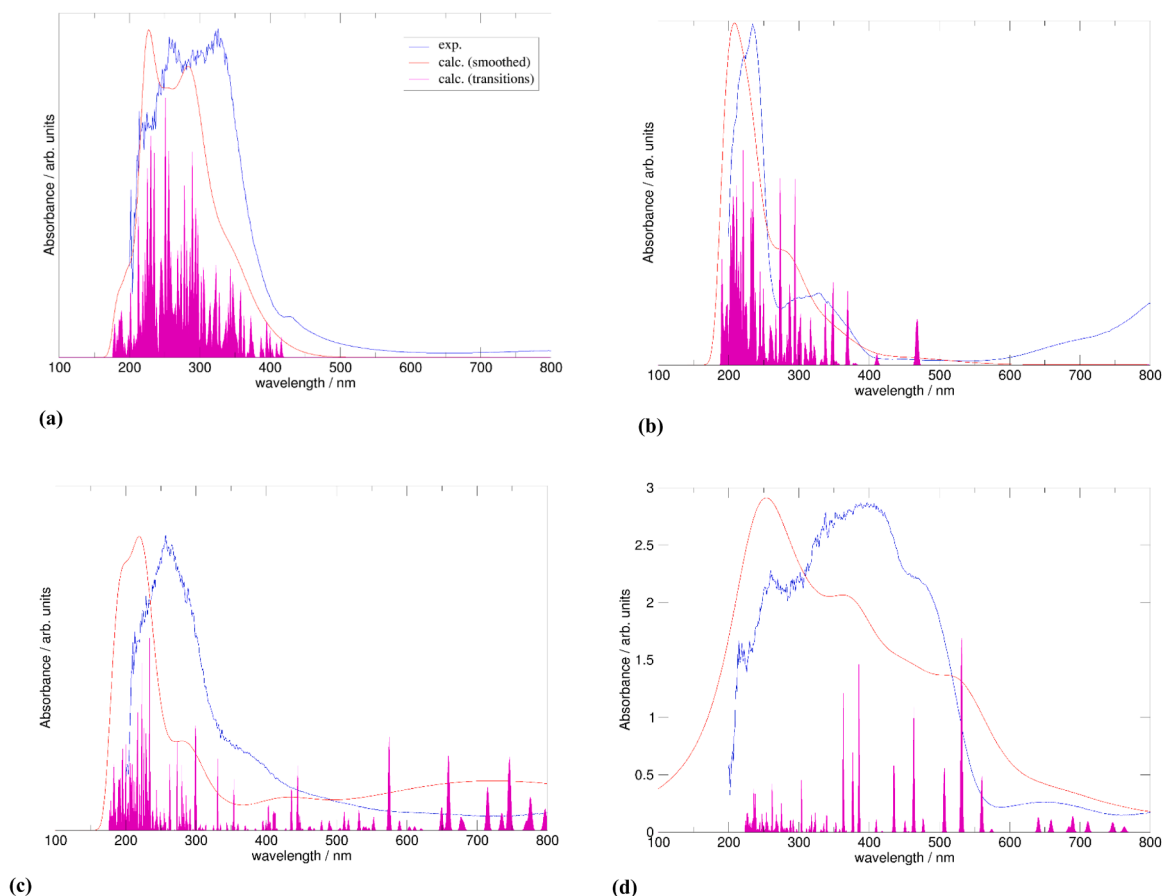


Fig. 2. Experimental UV-Vis spectra of: (a) Fe^{3+} -phosphate; (b) Fe^{2+} -sulphate; (c) siderite ($\text{Fe}^{2+}\text{CO}_3$); (d) goethite ($\text{Fe}^{3+}\text{O}(\text{OH})$) (blue lines) with TD-DFT spectra (red lines) and TD-DFT transitions (magenta spikes). Legend: blue line = experimental pattern; red line = calculated pattern; magenta bars = calculated transitions.

from compounds with different iron structures. These data enabled us to build a solid theoretical basis on the MCR predictive models. Unfortunately, ab initio calculations cannot be used alone to calculate and reproduce the spectra of the real samples because of the complexity of the multiple atom-atom interactions which makes the calculation time too lengthy.

3.2. Preliminary analysis of the UV-Vis spectra

This preliminary analysis enabled us to reveal correlations and clustering trends of the various parameters calculated from the raw, normalized, and first derivative UV-Vis with iron oxidation state and nuclearity. Specifically, the best correlation trend highlighting a distribution of points dependent on the nuclearity was obtained by plotting the wavelength corresponding to the maximum of the most intense absorption band (top absorption band) of the normalized data vs. the mean Kubelka-Munk (KM) value of the whole normalized spectrum (Fig. 3). Fig. 3a is the plot for Fe^{2+} , while Fig. 3b is the plot for Fe^{3+} . As a reference, both plots report the position of the magnetite sample (black square) which contains clusters of ferrous and ferric iron. Samples with isolated ferrous iron have small mean KM values and top absorption band positions of < 257 nm. On the other hand, samples with various clusters of ferrous iron have mean KM values of > 0.196 and top absorption band positions of > 257 nm (Fig. 3a). Correspondingly, samples with isolated ferric iron have mean KM values of < 0.4 and top absorption band positions of < 380 nm, while samples with various clusters of ferric iron have mean KM values > 0.46 and positions top absorption band positions of > 387 nm (Fig. 3b).

3.3. MCR analysis

This analysis revealed distinct clusters formed by samples with isolated Fe^{2+} , isolated Fe^{3+} , $\text{Fe}^{2+} + \text{Fe}^{3+}$ clusters, and pure Fe^{3+} cluster, based on the concentration values of the resolved components from the UV-Vis absorbance spectra. The best results were obtained with a four component MCR model (explaining 98% of data variance). The pure resolved spectral profiles are shown in Fig. 4. The resolved spectral profile corresponding to the first component (S1) shows an intense absorption band centred at about 350 nm and a very low intensity band at about 700 nm. This profile matches well the spectral profile of isolated Fe^{3+} , as it can be compared with the UV-vis spectra of FePO_4 , $\text{Fe}_2(\text{SO}_4)_3$ and $(\text{NH}_4)_3[\text{Fe}(\text{C}_2\text{O}_4)_3]$. The second (S2) and third (S3) component spectral profiles can be matched to the Fe^{3+} cluster structure. In particular, S3 shows an almost continuous absorption in the 200–600 nm range, which can be considered representative of all Fe^{3+} cluster structures. The spectral profile of the pure Fe^{3+} cluster is very similar, while S2 seems to model the specific behaviour of magnetite, where both Fe^{3+} and Fe^{2+} clusters are present, which also shows a continuous absorption in the 600–800 nm. Finally, the fourth component (S4) shows an intense band centred at about 250 nm, which is a characteristic absorption band of isolated Fe^{2+} structures, such as FeSO_4 and olivine.

Fig. 5a reports the scatter plot of the relative concentration third (C3) vs. first (C1) component, where each sample is coloured according to the iron form (see figure legend for details), and the grey filled circles correspond to the test samples (predicted). The Fe^{3+} cluster, including hematite, (in the left upper corner, high values in component 3 and low in component 1) is distinct from the isolated Fe^{3+} (in the right bottom corner, high C1 and low C3 values) with ammonium iron oxalate

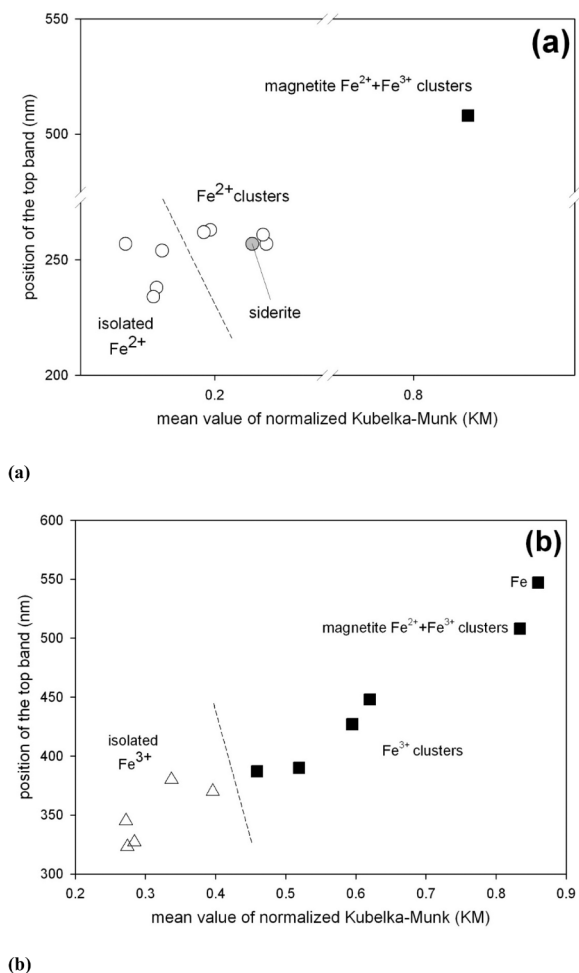


Fig. 3. Plot of the empirical correlation between the mean Kubelka-Munk (KM) value of the normalized data and the position (nm) of the top absorption band of the normalized data. (a) Fe^{2+} -rich samples; (b) Fe^{3+} -rich samples. The plots include the position of the magnetite sample (black square) which contains clustered iron atoms with both ferrous and ferric state. See text for details.

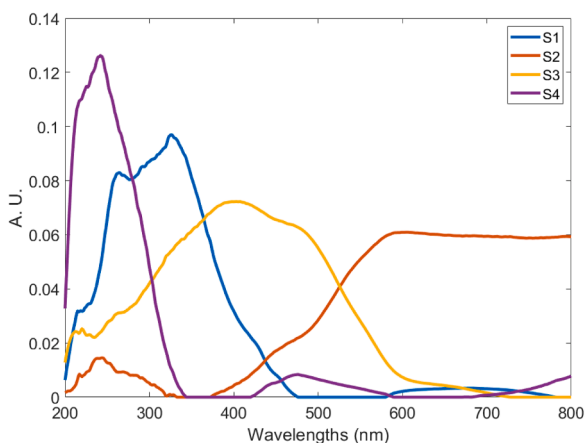


Fig. 4. The four pure resolved spectral profiles obtained from the MCR-ALS model.

trihydrate, iron sulfate hydrate, and iron phosphate dehydrate. Fig. 5b, C4 vs. C1 isolates (upper left corner) the samples well in which iron is bivalent (Fe^{2+}) with ammonium iron sulfate dodecahydrate and iron sulfate heptahydrate. An overall view is shown in the three-dimensional

scatter plot (Fig. 5c, reporting C1 vs. C3 vs. C4), where it is easier to assess which group the test samples are the most similar to.

Regarding the nuclearity in the samples of mineral fibres, actinolite asbestos from Aurina Valley, Bolzano (Italy) exhibits an intermediate behaviour between isolated Fe^{2+} (nuclearity = 1) and cluster iron (nuclearity > 2). This finding is in agreement with the outcome of the structure refinement reported in Pollastri et al. [57] where the octahedral sites $M(1)$, $M(2)$ and $M(3)$ are occupied by iron atoms, with Fe^{2+} ions (87%) occurring at the $M(1,2,3)$ sites and the small amount of Fe^{3+} (13%) ordered at the $M(2)$ site.

Amosite from Penge mine (Northern Province, South Africa) and the UICC standard crocidolite (South Africa) are anomalous because they are included in the family of samples with cluster iron (nuclearity > 2), but their position is shifted towards the groups of isolated iron. Literature data confirm that the nuclearity of iron in UICC crocidolite has to be > 2. This is because the three OH bands in the FTIR spectrum show that the association of three iron ions (lower frequency band at 3619 cm^{-1}) is much more abundant than that of two iron ions and one magnesium atom (3635 cm^{-1}), while the associations of two Mg atoms and one iron ion (3649 cm^{-1}) are low in abundance [45]. The UICC standard anthophyllite asbestos from Paakkila (Finland) is included in the family of samples with cluster iron (nuclearity > 2) because the investigated sample contains colloidal impurities of iron hydroxides inter-grown within the fibres, as also observed under the stereomicroscope (see Supplementary Information 3) and the signal comes mostly from these colloids.

These phases are amorphous in diffraction as they were not detected by the quantitative phase analysis reported in Pollastri et al. [60], where the results of the structure refinement indicated Fe^{2+} at the $M4$ distorted octahedral site. Chrysotile from the Balangero mine (Turin, Italy) exhibits prevalent isolated Fe^{2+} (nuclearity = 1). This result is in line with the model obtained from X-ray Absorption Spectroscopy [56] where low amounts of iron atoms (both Fe^{2+} and Fe^{3+}) are mainly found in an octahedral environment.

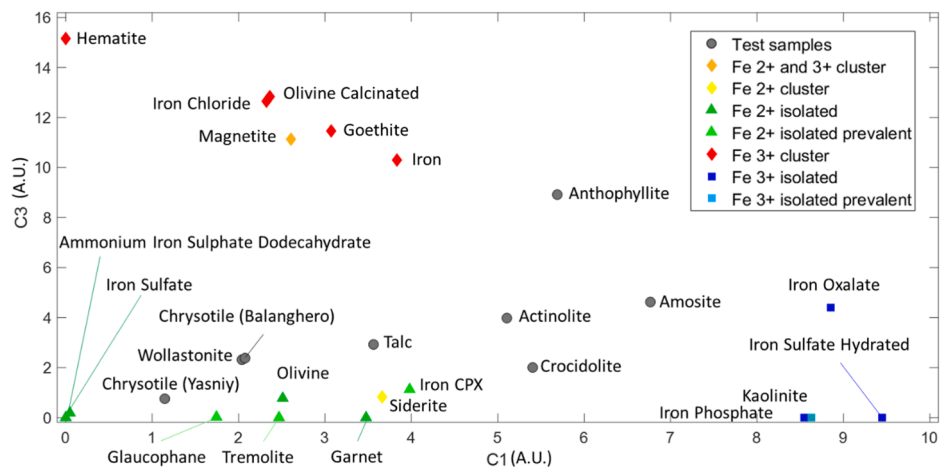
The commercial chrysotile from Yasniy mine, Orenburg Minerals (Russia) also exhibit prevalent isolated Fe^{2+} (nuclearity = 1). In agreement, Di Giuseppe et al. [12] found a low content of Fe^{2+} in Yasniy ($\text{Fe}^{2+}/\text{Fe}^{3+} = 0.61$) with Fe^{3+} mainly associated with magnetite impurities.

Fibrous glaucophane from San Anselmo, Marin County (CA, USA) displays prevalent isolated Fe^{2+} (nuclearity = 1). This result is in contrast with the data reported in Di Giuseppe et al. [14] where the analysis of FTIR spectra interpreted as bands generated by $\text{Mg-Fe}^{2+}\text{-Fe}^{2+}\text{-OH}$ and $\text{Fe}^{2+}\text{-Fe}^{2+}\text{-Fe}^{2+}\text{-OH}$ clusters, the $\text{Fe}^{3+}=0.70$ a.f.u. vs. $\text{Fe}^{2+}=1.31$ a.f.u. ratio and the existence of iron-amphibole impurities in the sample pointed to a nuclearity > 2. One explanation could be that the sample investigated here, which was selected under the optical microscope, is actually pure and that the bands generated by $\text{Mg-Fe}^{2+}\text{-Fe}^{2+}\text{-OH}$ and $\text{Fe}^{2+}\text{-Fe}^{2+}\text{-Fe}^{2+}\text{-OH}$ clusters are subordinated to $\text{Mg-Mg-Fe}^{2+}\text{-OH}$ bands in the FTIR spectra indicative of a prevalent isolated Fe^{2+} (nuclearity = 1).

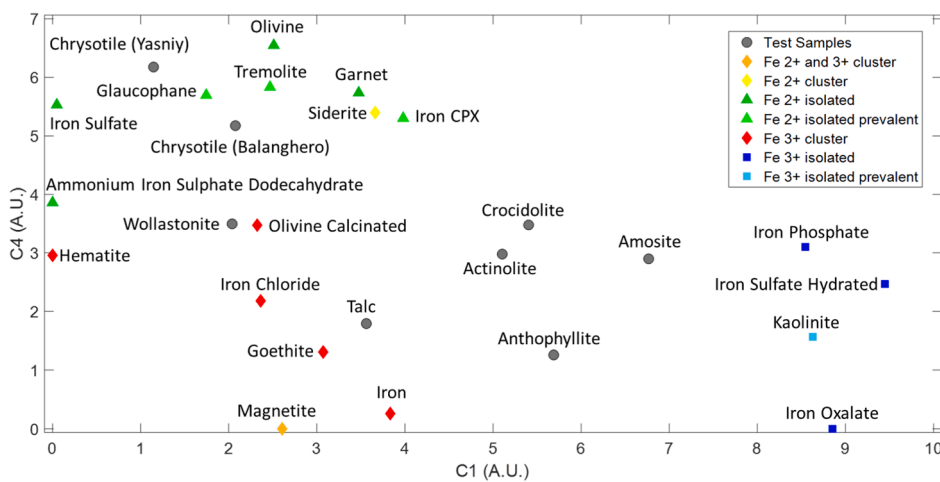
The sample of tremolite asbestos from the Lanzo Valley (Piedmont, Italy) is also included in the family of samples with isolated Fe^{2+} (nuclearity = 1). According to Pacella et al. [50], a minor amount of iron ($\text{Fe}^{3+}=0.05$ a.f.u. and $\text{Fe}^{2+}=0.24$ a.f.u. from the structure refinement) is found in the octahedral sites with Fe^{2+} at $M(1)$ and $M(3)$ confirmed by the FTIR spectrum. Commercial fibrous wollastonite NYAD G from Willsboro-Lewis (New York, USA) is also included in the family of samples with isolated Fe^{2+} (nuclearity = 1). The point is slightly shifted towards the other groups because Fe^{2+} prevails but significant Fe^{3+} is also present in the sample ($\text{FeO} = 0.33(0.09)$ wt% and $\text{Fe}_2\text{O}_3 = 0.17(0.09)$ wt%) [13].

3.4. Validating the relationship between iron nuclearity and toxicity

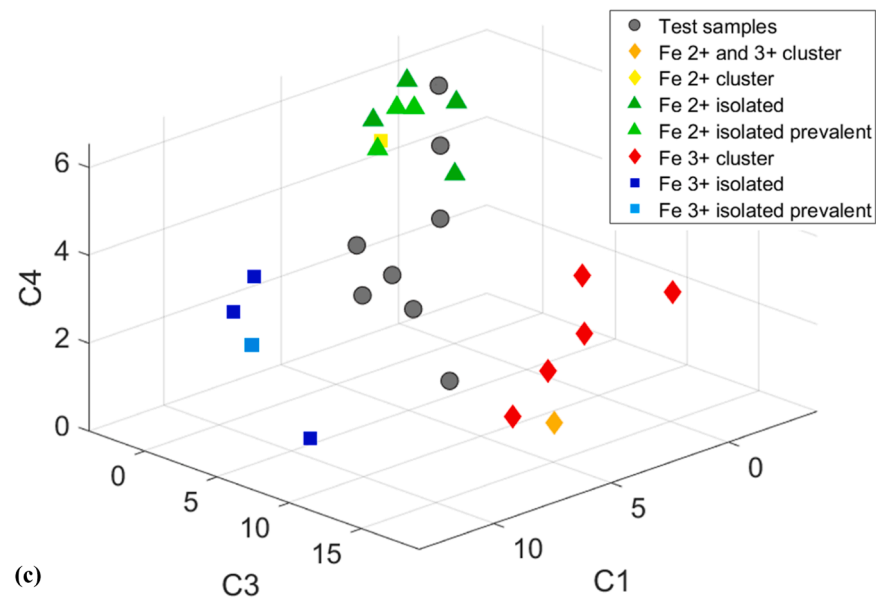
Iron has many different biological roles which are not yet fully



(a)



(b)



(c)

Fig. 5. Scatter plots of MCR components: (a) C1 vs C3, (b) C1 vs C4 and (c) C1 vs C3 vs C4.

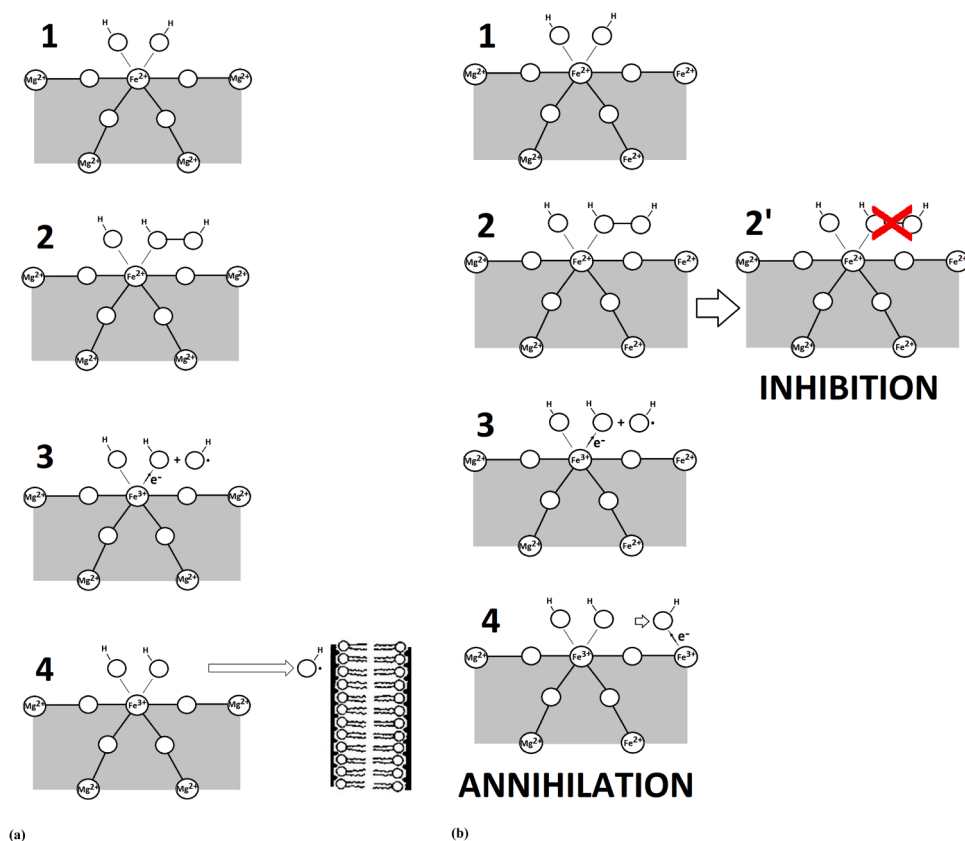


Fig. 6. (a) the case with Fe^{2+} nuclearity = 1. HO^{\bullet} can be produced by the interaction with H_2O_2 (steps 2 and 3). The produced HO^{\bullet} can move beyond the first shells of iron and cause damage to nearby proteins, DNA or membranes (step 4). (b) the case with Fe^{2+} nuclearity > 1. The produced HO^{\bullet} (steps 2 and 3) interacts with other iron atoms in the second shell by oxidizing them and producing OH^- species (annihilation of the HO^{\bullet} , step 4). In this case, the produced HO^{\bullet} is not capable of causing biological damage. A possible alternative is the inhibition itself (step 2') of the production of HO^{\bullet} (see text for details).

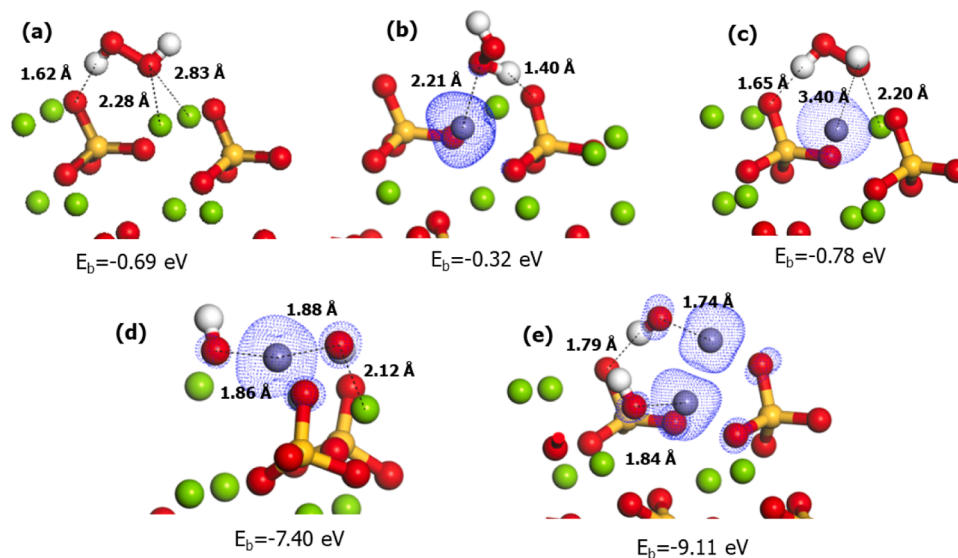


Fig. 7. Final optimized structures of the hydrogen peroxide molecule on the forsterite surfaces with 0 (a), 1 (b,c,d) and 2 (e) Fe^{2+} ions. The binding energies of the reaction surface model + H_2O_2 is also reported. The distances between atoms of the H_2O_2 molecule interacting with Mg^{2+} and Fe^{2+} ions are highlighted with dashed lines and labelled with the numerical values. The spin density is also reported as dotted blue iso-surfaces.

understood. On the one hand, it can significantly increase the activity of antioxidant agents, resulting in the inhibition of free radical formation (see for example, [2,3]). On the other, iron plays a role in inducing adverse effects in vivo via the production of HO^{\bullet} . Toyokuni [66] underlined the role of iron in carcinogenesis as a ferrototoxic disease and

the detrimental action of iron was confirmed by the finding that the iron chelators inhibit HO^{\bullet} formation [28,29,35].

The basic assumption of our work is that the nuclearity of iron affects the toxicity of a mineral particle/fibre. This hypothesis relies on the observations that fibre activity has to be dependent on iron that has

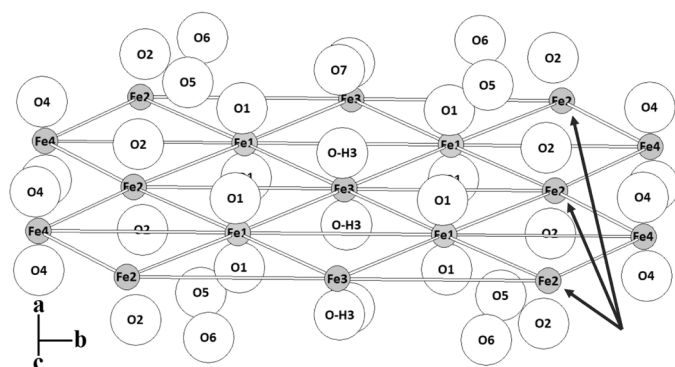


Fig. 8. A sketch of the structure of iron-rich asbestos amphiboles amosite and crocidolite plotted in the *b-c* plane showing the iron sites Fe1 =*M*(1), Fe2 =*M*(2), Fe3 =*M*(3), and Fe4 =*M*(4) coordinated by oxygen atoms (O1 to O6) in octahedral coordination. Si and H atoms are omitted. Mg atoms may occupy the same octahedrally coordinated sites in place of the iron atoms. The white lines connect neighbour (second shell) iron atoms and evidence the high nuclearity of the iron atoms (Fe1 =6, Fe2 =5, Fe3 =6, and Fe4 =3) eventually reduced by the presence of Mg atoms.

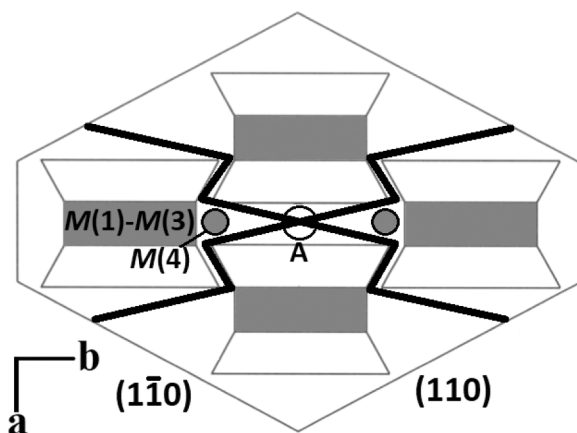


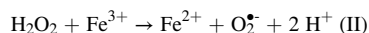
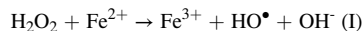
Fig. 9. Preferred cleavage directions [15], represented by the black lines, that break the crystal fibres in such a way to expose the *M*(4) (active for catalytic activity) and A sites at the surface. The A sites are usually occupied by Na⁺ and K⁺ ions or are empty.

attained a particular location at the crystal surface [22]. In addition, disperse iron ions are more effective in the catalysing generation of toxic oxidant species such as HO[•] than iron clusters [28,29].

The literature describes the “nuclearity effects” of iron well (see for example, [46,9]). Iron-free synthetic chrysotile elicited a negligible HO[•] generation and was non-toxic in cellular tests. When doped with Fe³⁺, synthetic chrysotile induced cytotoxic effects in murine alveolar macrophages and acquired the ability to generate free radicals in acellular systems [20,21]. The results of Andreozzi et al. [6] on amphibole asbestos are in line with previous results on iron-doped synthetic chrysotile, and indicate that the highest reactivity in asbestos is associated with the occurrence of low-coordinated, low-nuclearity iron sites. Newly-formed iron-rich nanoparticles are poorly reactive in redox cycles and do not modulate the overall crocidolite radical reactivity due to the high nuclearity of the iron centres and the stability of the structural coordinative ligands [46]. When the nuclearity of iron increases, as observed in iron oxides, catalytic activity decreases. Freyria et al. [18] observed that hematite microparticles did not produce hydroxyl radicals. Lee and Park [40] reported that hematite can be used as a catalyst for the Fenton reaction by the change in the redox state of iron ions on its

surface. However, existing hematite-based photocatalysts exhibit high hole–electron recombination due to the narrow bandgap and limited ROS production.

The question thus arises as to why single, or low nuclearity iron atoms are more prone to catalytically produce free radicals and hence to make the fibre potentially more toxic than iron clusters with high nuclearity. Fe³⁺ in the oxidized surface of the fibres can be reduced when the fibres are engulfed in the acidic intracellular phagolysosomes where Fe²⁺ is stable [38] and whose toxicity is considered much greater than that of Fe³⁺. In fact, although both Fe²⁺ and Fe³⁺ produce HO[•] via Fenton reactions (I) and (II):



the latter being several orders of magnitude slower than the former (0.002 M⁻¹s⁻¹ vs. 60 M⁻¹s⁻¹: [65]), causing rapid Fe³⁺ accumulation and precipitation [43]. Because in the intracellular phagolysosome vacuoles, there is an excess of H₂O₂, we can assume the radical pathway of the Fenton reaction and an inner-sphere reaction where a Fe²⁺-ligand like water must make room for H₂O₂ before ⁻ transfer [38].

If Fe²⁺ has nuclearity= 1 and is surrounded only by atoms other than iron/metals (e.g. Mg²⁺) (step 1 in Fig. 6a), it may produce HO[•] by the interaction with H₂O₂ (steps 2 and 3 in Fig. 6a). Although the HO[•] produced has a very short life [23], it is free to move beyond the first shells of iron, does not meet catalytically active species, and thus does not damage nearby proteins, DNA or membranes (step 4 in Fig. 6a).

If Fe²⁺ has nuclearity > 1 (e.g. nuclearity=3 in step 1 of Fig. 6b), it produces HO[•] (steps 2 and 3 in Fig. 6b) that promptly interacts with other catalytically active iron/metal atoms in the second shell by oxidizing them and producing OH⁻ species (annihilation of the HO[•] as shown by step 4 in Fig. 6b). Hence the HO[•] produced is unable to cause any biological damage and shows little to null toxicity. A possible alternative mechanism is the inhibition itself of the production of HO[•] (inhibition in step 2' in Fig. 6b) by iron when nuclearity increases.

To gain some insights into the effect of nuclearity on H₂O₂ splitting, we performed DFT calculations of H₂O₂ interacting with models of forsterite (010) surface terminated with Mg²⁺ ions in which 1 or 2 Mg²⁺ ions were substituted with Fe²⁺ ions. (Fig. S2 of the Supplementary Information 2). Note that we considered (Fe↔Mg) substitutions in the modelling of these structures because (Fe,Mg) vicariance is very common in mineral fibres (see for example the serpentine asbestos chrysotile with (Mg,Fe)₃(OH)₄Si₂O₅ or the amphibole asbestos fibre amosite Na₂(Fe,Mg)₅Si₈O₂₂(OH)₂, crocidolite Na₂(Fe,Mg)₅Si₈O₂₂(OH)₂, and tremolite Ca₂(Mg,Fe)₅Si₈O₂₂(OH)₂).

Our calculations revealed that H₂O₂ absorbs molecularly on the model without iron atoms (pure forsterite) with a binding energy of −0.69 eV. In the final geometry shown in Fig. 7a, 1 oxygen of H₂O₂ interacts with Mg²⁺ with a distance of 2.28 Å, whereas the hydrogen bonded to the other oxygen of the H₂O₂ molecule forms a hydrogen bond of 1.62 Å with the oxygen of a SiO₄ unit nearby. Regarding the interaction of H₂O₂ in the model with 1 Fe²⁺ ion, we observed how molecular adsorption or breaking of the O–O bond depended on how we docked the molecule on the surface. When the molecule was adsorbed physically, we computed a binding energy ranging between −0.32 to −0.78 eV depending on the interaction mode as shown in Fig. 7b and c. When the molecule was positioned with the two oxygens interacting with the Fe²⁺ and Mg²⁺ ions close together, hydrogen peroxide splitting occurred. The two hydroxyl groups bridged the two ions.

Fig. 7 also reports the spin density, showing that whereas in the case of molecular adsorption only the iron ion bears a spin density, when the hydrogen peroxide splits, a small spin density is localized on both hydroxyls, thus denoting a small radical character on both groups. The reaction is exothermic with −7.4 eV.

Lastly, on the model containing 2 iron ions, we observed only the splitting reaction as shown in Fig. 7e. Again, the spin density is localized

on the two iron ions and the two oxygens of the hydroxyl groups. The Fe^{3+} -OH bonds lie in the range 1.7–1.9 Å and the reaction energy is strongly exothermic with the release of about -9.1 eV. We should emphasize that our calculations were performed in a vacuum and with a static approach, and they thus neglect important solvents and dynamical effects that would certainly affect the geometry and energy of the adsorption and splitting reactions. However, they still provide useful insights and suggest that iron plays a key role in splitting H_2O_2 and in the fate of the hydroxyl groups. Despite the aforementioned limitations, these simple calculations seem to indicate that the HO^\bullet group has some kind of annihilation mechanism (Fig. 6b).

3.5. From the MCR model to the FPTI nuclearity-related toxicity parameters

The findings from the MCR model can be used to predict the FPTI nuclearity-related toxicity parameter of mineral fibres [24], however it should be noted that iron nuclearity is only one of the 18 parameters of the FPTI model. In the present work its effect is thus combined with that of the other 17 fibre parameters (length, width, crystal curvature, crystal habit, density, character of the surface, surface area, total iron content, ferrous iron, content of metals other than iron, dissolution rate, velocity of iron release, velocity of silica dissolution, velocity of release of metals, zeta potential, fibre aggregation, and cation exchange). To predict the FPTI nuclearity-related toxicity parameter (1,10) from the MCR model, the following steps are necessary:

- Preparation of as pure a sample as possible, separating the fibres from impurities by manual selection under an optical microscope, and grinding the purified sample in agate mortar or with cryomilling;
- Collection of the UV-Vis spectrum in the 200-800 nm range using the same experimental conditions employed here to measure the standard samples;
- Spectra normalization;
- Use of the derived MCR model to predict the values of the components C1, C2, C3 and C4 for the sample;
- Classification of the sample based on the values of the four components C1 to C4. High values of C1 = isolated Fe^{3+} ; high values of C2 = cluster Fe^{2+} and Fe^{3+} ; high values of C3 = cluster Fe^{3+} ; high values of C4 = isolated Fe^{2+} . Intermediate values of both C1 and C3 are also possible and interpreted as iron with low nuclearity;
- Assignment of the value of the nuclearity-related toxicity parameter 1.10 in the FPTI model [24,25] with:

High values of the component C1 (isolated Fe^{3+}) or C4 (isolated Fe^{2+}) \rightarrow iron nuclearity = 1 \rightarrow index value = 0.07 (high toxicity, due to the higher probability of producing HO^\bullet);

Intermediate values of both C1 and C3 or C2 and C4 \rightarrow iron nuclearity = 2 \rightarrow index value = 0.03 (low-moderate toxicity);

High values of the component C2 (cluster Fe^{2+} and Fe^{3+}) or C3 (cluster Fe^{3+}) \rightarrow iron nuclearity > 2 \rightarrow index value = 0.02 (low toxicity).

For the investigated mineral fibres, a value of 0.07 of the nuclearity-related toxicity parameter in the FPTI model [24], corresponding to high C4 values (isolated Fe^{2+}), was assigned to the Balangero mine (Italy) and commercial Yasnyy (Russia) chrysotiles, fibrous glaucophane from California, asbestos tremolite from Piedmont (Italy) and commercial fibrous wollastonite NYAD G (USA). A value of 0.03 was assigned to actinolite asbestos from Aurina Valley (Italy), amosite from Penge (South Africa), and UICC crocidolite because these fibres exhibit high intermediate values (Fig. 5a,b). A value of 0.02 corresponding to high C3 values (cluster Fe^{3+}) was assigned to UICC asbestos anthophyllite from Finland. These data revise the previous qualitative assessments of chrysotile from the Balangero mine (Italy) with 0.03 the commercial Yasnyy (Russia) chrysotile with 0.03 fibrous glaucophane from California with 0.02, and asbestos tremolite from Piedmont (Italy) with 0.03 ([14], 2012a).

Some samples were difficult to classify since their position in the MCR relative concentration plots (Fig. 5) was either close to samples with different nuclearity or else it fell between two different groups. The iron-rich amphibole asbestos amosite and crocidolite are an example of anomalous spots as they are included in the family of samples with cluster iron (nuclearity > 2); however, their position is shifted towards the groups of isolated iron. Fig. 8 depicts the position of iron ($\text{Fe1} = M(1)$, $\text{Fe2} = M(2)$, $\text{Fe3} = M(3)$, and $\text{Fe4} = M(4)$) octahedrally coordinated oxygen atoms (O1 to O6) in the monoclinic structure of these amphiboles.

Ideally, an iron atom in the Fe1 site has six neighbour iron atoms (see the white lines in the figure), Fe2 site has five, Fe3 site has six atoms, and Fe4 site has three. A possible explanation of the shift towards the cluster of isolated iron atoms is that if Mg atoms, which are invariably present in the structure of these amphiboles in place of the iron atoms, occupy the Fe2 site (indicated by the black arrow), the iron atom is left isolated in the Fe4 site. The same may occur if, for example, Fe1 and Fe2 are simultaneously occupied by Mg atoms, leaving the iron atom in Fe3 isolated.

The catalytic activity of isolated Fe4 atoms in the $M(4)$ site of amphiboles is very important as this is the site exposed at the surface of the crystal fibres they cleave. In fact, the preferred cleavage plane [15], represented by the black lines in Fig. 9, breaks the crystal fibres in such a way to leave $M(4)$ sites at the surface next to A sites, usually occupied by alkaline ions.

The exception represented by the siderite sample also needs highlighting. Its observed and calculated spectra seem to point to a case of isolated Fe^{2+} , however the siderite structure [17] exhibits a nuclearity equal to 6. Each Fe^{2+} atom has 6 Fe^{2+} neighbours connected by oxygen atoms in the second shell at ca. 4.28 Å (as the calculated Fe-O bond distance is 2.14 Å) with a hexagonal packing similar to that of hematite. The only difference with respect to hematite is that carbon atoms are also found in the oxygen atoms' trigonal cavity and hence help shield Fe^{2+} atoms from Fe^{2+} neighbours. A possible explanation of its outlier behaviour is that carbonate anions may prevent states localized on the iron cations from interacting with each other, effectively isolating each Fe^{2+} centre from one another, at least from the point of view of the electronic density of states (eDOS).

The spread of the predicted samples with respect to the identified clusters may also be due to the contribution of residual iron-rich impurities in the natural samples to the overall UV-Vis spectrum. One example is the anthophyllite asbestos from Finland which contains inseparable colloidal impurities of iron hydroxides inter-grown within the fibre bundles (see Fig. S3 in the Supplementary Information 3). Although they were clearly separate under the optical microscope, the chrysotile fibres of the Russian sample may still contain residual nanophase magnetite crystals. On the other hand, the chrysotile fibres from Balangero (Italy) may still contain slight residual impurities of iron-rich phases such as antigorite, balangeroite, clinocllore, magnetite, and talc, as reported in Pollastri et al. [55,59].

4. Conclusions

Iron catalytic properties, determined by the oxidation state and nuclearity, prompt the Fenton primary production of cyto-/geno-toxic hydroxyl radical HO^\bullet , which is responsible for the toxicity and carcinogenicity of respirable mineral fibres. For what we believe is the first time, the iron nuclearity of mineral fibres has been systematically investigated in this work in an attempt to quantitatively assess its contribution to the FPTI predictive model of the toxicity and carcinogenicity of mineral fibres.

As a first step, ab initio calculations by density functional theory (DFT) modelling were used in order to interpret the origin of most of the observed bands in the UV-Vis spectra of mineral fibre standards. Ab initio calculations were also used to investigate the hydrogen peroxide adsorption, responsible for the production of HO^\bullet radicals, on olivine-like surfaces reproducing an ideal fibre surface. We demonstrated that the increase in Fe^{2+} nuclearity effectively decreases the toxicity

potential because HO[•] radicals are directly annihilated due to the oxidation of Fe²⁺ to Fe³⁺.

As a second step, we applied empirical models, using the multivariate curve resolution (MCR) approach to obtain quantitative information on iron nuclearity from UV-Vis spectra in the 200–800 nm region and classify the iron nuclearity of all the investigated mineral fibres. The empirical model enabled the computation of a high nuclearity-related toxicity parameter (0.07) for the chrysotile samples from the Balangero mine (Italy), commercial chrysotile from Yasniy (Russia) chrysotiles, fibrous glaucophane from California, asbestos tremolite from Piedmont (Italy) and commercial fibrous wollastonite NYAD G (USA). Intermediate values of toxicity (0.03), corresponding to a mean nuclearity of 2, were assigned to actinolite asbestos from Aurina Valley (Italy), amosite from Penge (South Africa), and UICC crocidolite. Conversely, a low nuclearity-related toxicity parameter (0.02), corresponding to iron-cluster with a lower catalytic capacity of producing oxidants, was assigned to UICC asbestos anthophyllite from Finland.

We acknowledge that the statistical robustness of our MCR data could be improved in order to reduce the scatter in the distribution of the points within the cluster. This scatter is mainly due to the residual iron-rich impurities present in natural samples such as the anthophyllite asbestos from Finland and the chrysotile fibres which may still contain residual nanophasic magnetite crystals or iron-rich phases such as antigorite, balangeroite, clinocllore, magnetite, and talc.

Understanding iron nuclearity contributes to improving the FPTI model which considers all the physical-crystal-chemical parameters of a mineral fibre. Of these, the activity of metals such as magnesium, the vicariant of iron in the crystal structure of mineral fibres, is also included in the FPTI model as it is important for (i) mineral fibres such as chrysotile whose fast dissolution [28,29,31] in contact with acidic phagolysosomes, during macrophage phagocytosis, promotes the release of haemolytic magnesium species; (ii) systems showing the corrosion of magnesium-rich surfaces (see for example, [33]) and the release of this metal in vitro.

Environmental implications

The environmental implications of this work regard the understanding of the role of iron present in mineral fibres in inducing toxic (acute and chronic) and pathogenic effects in vivo via production of oxidant species. The method proposed here is aimed at determining the chemical environment and nuclearity of iron in mineral fibres (asbestos and non-asbestos species) as a factor to predict and classify their toxicity/carcinogenicity potential.

CRedit authorship contribution statement

Marina Cocchi: Writing – review & editing, Writing – original draft, Supervision, Methodology. **Alessandro Francesco Gualtieri:** Writing – review & editing, Writing – original draft, Supervision, Project administration, Methodology, Investigation, Funding acquisition, Formal analysis, Data curation, Conceptualization. **Elena Castellini:** Writing – review & editing, Supervision, Investigation. **Lorenzo Strani:** Writing – original draft, Software, Investigation, Formal analysis, Data curation, Conceptualization. **Alfonso Pedone:** Writing – review & editing, Writing – original draft, Visualization, Methodology, Investigation, Formal analysis. **Francesco Muniz-Miranda:** Writing – review & editing, Writing – original draft, Methodology, Investigation, Formal analysis.

Declaration of Competing Interest

The authors declare that they have no known competing financial interests or personal relationships that could have appeared to influence the work reported in this paper.

Data Availability

Data will be made available on request.

Acknowledgments

The work is supported by the PRIN project fund “Fibres: a multi-disciplinary mineralogical, crystal-chemical and biological project to amend the paradigm of toxicity and cancerogenicity of mineral fibres” (PRIN: Progetti di Ricerca di Rilevante Interesse Nazionale—Bando 2017—Prot. 20173X8WA4). M. Vaccari, D. Di Giuseppe and V. Scognamiglio are kindly acknowledged for their support in the data collection of the UV-Vis spectra. A. Cornia is kindly acknowledged for fruitful discussions. The author wishes to thank the three competent referees of the paper for their constructive revision.

Appendix A. Supporting information

Supplementary data associated with this article can be found in the online version at [doi:10.1016/j.jhazmat.2024.134004](https://doi.org/10.1016/j.jhazmat.2024.134004).

References

- [1] Agustina, E., Goak, J., Lee, S., Seo, Y., Park, J.Y., Lee, N., 2015. Simple and precise quantification of iron catalyst content in carbon nanotubes using UV/Visible spectroscopy. *Chem Open* 4 (5), 613–619.
- [2] Akhavan, O., Ghaderi, E., Rahimi, K., 2012. Adverse effects of graphene incorporated in TiO₂ photocatalyst on minuscule animals under solar light irradiation. *J Mater Chem* 22 (43), 23260–23266.
- [3] Akhavan, O., Kalaei, M., Alavi, Z.S., Ghiasi, S.M.A., Esfandiari, A., 2012. Increasing the antioxidant activity of green tea polyphenols in the presence of iron for the reduction of graphene oxide. *Carbon* 50 (8), 3015–3025.
- [4] Akhavan, O., Hashemi, E., Zare, H., Shamsara, M., Taghavinia, N., Heidari, F., 2016. Influence of heavy nanocrystals on spermatzoa and fertility of mammals. *Mater Sci Eng: C* 69, 52–59.
- [5] Alimirzaei, F., Kieslich, C.A., 2023. Machine learning models for predicting membranolytic anticancer peptides. *Comput Aided Chem Eng* 52, 2691–2696.
- [6] Andreozzi, G.B., Pacella, A., Corazzari, I., Tomatis, M., Turci, F., 2017. Surface reactivity of amphibole asbestos: a comparison between crocidolite and tremolite. *Sci Rep* 7 (1), 1–9.
- [7] Becke, D., 1993. Density-functional thermochemistry. III. The role of exact exchange. *J Chem Phys* 98, 5648–5652 doi: 10.1063/1.464913.
- [8] Borghi, E., Occhiuzzi, M., Foresti, E., Lesci, I.G., Roveri, N., 2010. Spectroscopic characterization of Fe-doped synthetic chrysotile by EPR, DRS and magnetic susceptibility measurements. *Phys Chem Chem Phys* 12 (1), 227–238.
- [9] Bu, F., Chen, C., Yu, Y., Hao, W., Zhao, S., Hu, Y., Qin, Y., 2023. Boosting Benzene Oxidation with a Spin-State-Controlled Nuclearity Effect on Iron Sub-Nanocatalysts. *Angew Chem Int Ed* 62 (3), e202216062.
- [10] De Juan, A., Tauler, R., 2021. Multivariate Curve Resolution: 50 years addressing the mixture analysis problem – A review. *Anal Chim Acta* 1145, 59–78.
- [11] Demichelis, R., Bruno, M., Massaro, F.R., Principe, M., De La Pierre, M., Nestola, F., 2015. First-principle modelling of forsterite surface properties: Accuracy of methods and basis sets. *J Comput Chem* 36 (19), 1439–1445 doi/ 10.1002/jcc.23941.
- [12] Di Giuseppe, D., Zoboli, A., Nodari, L., Pasquali, L., Sala, O., Ballirano, P., Malferrari, D., Raneri, S., Hanuskova, M., Gualtieri, A.F., 2021. Characterization and assessment of the potential toxicity/pathogenicity of Russian commercial chrysotile. *Am Min* 106 (10), 1606–1621.
- [13] Di Giuseppe, D., Scognamiglio, V., Malferrari, D., Nodari, L., Pasquali, L., Lassinanti Gualtieri, M., Scarfi, S., Mirata, S., Tessari, U., Hanuskova, M., Gualtieri, A.F., 2021. Characterization of fibrous wollastonite NYAD G in view of its use as negative standard for in vitro toxicity tests. *Minerals* 11 (12), 1378.
- [14] Di Giuseppe, D., Harper, M., Bailey, M., Erskine, B., Della Ventura, G., Ardit, M., Pasquali, L., Tomaino, G., Ray, R., Mason, H., Dyar, M.D., Hanuskova, M., Giacobbe, C., Zoboli, A., Gualtieri, A.F., 2019. Characterization and assessment of the potential toxicity/pathogenicity of fibrous glaucophane. *Environ Res* 178, 108723.
- [15] Dorling, M., Zussman, J., 1987. Characteristics of asbestiform and non-asbestiform calcic amphiboles. *Lithos* 20 (6), 469–489.
- [16] Dunning Jr., T.H., Hay, P.J., 1977. Gaussian Basis Sets for Molecular Calculations. In: Schaefer III, H.F. (Ed.), *Modern Theoretical Chemistry*, Vol. 3. Plenum, New York, pp. 1–28.
- [17] Effenberger, H., Mereiter, K., Zemann, J., 1981. Crystal structure refinements of magnesite, calcite, rhodochrosite, siderite, smithsonite, and dolomite, with discussion of some aspects of the stereochemistry of calcite type carbonates. *Z für Krist-Cryst Mat* 156 (1–4), 233–244.
- [18] Freyria, F.S., Bonelli, B., Tomatis, M., Ghiazza, M., Gazzano, E., Ghigo, D., Garrone, E., Fubini, B., 2012. Hematite nanoparticles larger than 90 nm show no sign of toxicity in terms of lactate dehydrogenase release, nitric oxide generation,

- apoptosis, and comet assay in murine alveolar macrophages and human lung epithelial cells. *Chem Res Tox* 25 (4), 850–861.
- [19] Frisch, M.J., Trucks, G.W., Schlegel, H.B., Scuseria, G.E., Robb, M.A., Cheeseman, J.R., Scalmani, G., Barone, V., Petersson, G.A., Nakatsuji, H., Li, X., Caricato, M., Marenich, A.V., Bloino, J., Janesko, B.G., Gomperts, R., Mennucci, B., Hratchian, H.P., Ortiz, J.V., Izmaylov, A.F., Sonnenberg, J.L., Williams-Young, D., Ding, F., Lipparini, F., Egidi, F., Goings, J., Peng, B., Petrone, A., Henderson, T., Ranasinghe, D., Zakrzewski, V.G., Gao, J., Rega, N., Zheng, G., Liang, W., Hada, M., Ehara, M., Toyota, K., Fukuda, R., Hasegawa, J., Ishida, M., Nakajima, T., Honda, Y., Kitao, O., Nakai, H., Vreven, T., Throssell, K., Montgomery, J.A., Jr., Peralta, J.E., Ogliaro, F., Bearpark, M.J., Heyd, J.J., Brothers, E.N., Kudin, K.N., Staroverov, V.N., Keith, T.A., Kobayashi, R., Normand, J., Raghavachari, K., Rendell, A.P., Burant, J.C., Iyengar, S.S., Tomasi, J., Cossi, M., Millam, J.M., Klene, M., Adamo, C., Cammi, R., Ochterski, J.W., Martin, R.L., Morokuma, K., Farkas, O., Foresman, J.B., Fox, D.J. 2016. *Gaussian 16 Rev. B. 01 Release Notes*.
- [20] Gazzano, E., Foresti, E., Lesci, I.G., Tomatis, M., Riganti, C., Fubini, B., Roveri, N., Ghigo, D., 2005. Different cellular responses evoked by natural and stoichiometric synthetic chrysotile asbestos. *Toxicol Appl Pharmacol* 206, 356–364.
- [21] Gazzano, E., Turci, F., Foresti, E., Putzu, M.G., Aldieri, E., Silvagno, F., Lesci, I.G., Tomatis, M., Riganti, C., Romano, C., Fubini, B., Roveri, N., Ghigo, D., 2007. Iron-loaded synthetic chrysotile: a new model solid for studying the role of iron in asbestos toxicity. *Chem Res Toxicol* 20, 380–387.
- [22] Gold, J., Amandusson, H., Krozer, A., Kasemo, B., Ericsson, T., Zanetti, G., Fubini, B., 1997. Chemical characterization and reactivity of iron chelator-treated amphibole asbestos. *Environ Health Persp* 105 (5), 1021–1030.
- [23] Goldstein, S., Meyerstein, D., Czapski, G., 1993. The fenton reagents. *Free Radic Biol Med* 15 (4), 435–445.
- [24] Gualtieri, A.F., 2018. Towards a quantitative model to predict the toxicity/pathogenicity potential of mineral fibres. *Toxicol Appl Pharm* 361, 89–98.
- [25] Gualtieri, A.F., 2021. Bridging the gap between toxicity and carcinogenicity of mineral fibres by connecting the fibre crystal-chemical and physical parameters to the key characteristics of cancer. *Curr Res Toxicol* 2, 42–52.
- [26] Gualtieri, A.F., Mossman, B.T., Roggli, V.L., 2017. Towards a general model for predicting the toxicity and pathogenicity of mineral fibres. *Eur Miner Union Notes Miner* 18, 501–532.
- [27] Gualtieri, A.F., Pollastri, S., Bursi Gandolfi, N., Lassinantti Gualtieri, M., 2018. *In vitro* acellular dissolution of mineral fibres: A comparative study. *Sci Rep* 8 (1), 7071.
- [28] Gualtieri, A.F., Andreozzi, G.B., Tomatis, M., Turci, F., 2019. Iron from a geochemical viewpoint. Understanding toxicity/pathogenicity mechanisms in iron-bearing minerals with a special attention to mineral fibres. *Free Radic Biol Med* 133, 21–37.
- [29] Gualtieri, A.F., Lusvardi, G., Zoboli, A., Di Giuseppe, D., Gualtieri, M.L., 2019. Biodurability and release of metals during the dissolution of chrysotile, crocidolite and fibrous erionite. *Environ Res* 171, 550–557.
- [30] Hardy, J.A., Aust, A.E., 1995. Iron in asbestos chemistry and carcinogenicity. *Chem Rev* 95 (1), 97–118.
- [31] Hume, L.A., Rimstidt, J.D., 1992. The biodurability of chrysotile asbestos. *Am Mineral* 77 (9-10), 1125–1128.
- [32] IUPAC, 2006. *Compendium of Chemical Terminology*, 3rd ed. International Union of Pure and Applied Chemistry. Online version 3.0.1, 2019 doi.org/10.1351/goldbook.NT06774.
- [33] Jafari, H., Heidari, E., Barabi, A., Dashti Kheirabadi, M., 2018. Effect of phase transformation during long-term solution treatment on microstructure, mechanical properties, and bio-corrosion behavior of Mg–5Zn–1.5 Y cast alloy. *Acta Metall Sin (Engl Lett)* 31, 561–574.
- [34] Jaumot, J., De Juan, A., Tauler, R., 2015. MCR-ALS GUI 2.0: New features and applications. *Chemom Intell Lab Syst* 140, 1–12. https://doi.org/10.1016/j.chemolab.2014.10.003.
- [35] Kamp, D.W., Weitzman, S.A., 1999. The molecular basis of asbestos induced lung injury. *Thorax* 54 (7), 638–652.
- [36] Kieslich, C.A., Alimirzaei, F., Song, H., Do, M., Hall, P., 2021. Data-driven prediction of antiviral peptides based on periodicities of amino acid properties. *Comput Aided Chem Eng* 50, 2019–2024.
- [37] Knipping, J.L., Behrens, H., Wilke, M., Göttlicher, J., Stabile, P., 2015. Effect of oxygen fugacity on the coordination and oxidation state of iron in alkali bearing silicate melts. *Chem Geol* 411, 143–154.
- [38] Koppel, W.H., Hider, R.H., 2019. Iron and redox cycling. *Do'S Don'ts Free Radic Biol Med* 133, 3–10.
- [39] Lee, C., Yang, W., Parr, R.G., 1988. Development of the Colle-Salvetti correlation-energy formula into a functional of the electron density. *Phys Rev B* 37, 785–789 doi 10.1103/PhysRevB.37.785.
- [40] Lee, S., Park, J.W., 2020. Hematite/graphitic carbon nitride nanofilm for fenton and photocatalytic oxidation of methylene blue. *Sustainability* 12 (7), 2866 doi 10.3390/su12072866.
- [41] Liang, S., Deng, X., Chang, Y., Sun, C., Shao, S., Xie, Z., Xiao, X., Ma, P., Zhang, H., Cheng, Z., Lin, J., 2019. Intelligent hollow Pt-CuS Janus architecture for synergistic catalysis-enhanced sonodynamic and photothermal cancer therapy. *Nano Lett* 19 (6), 4134–4145.
- [42] Lin, P.J., Yeh, C.H., Jiang, J.C., 2021. Theoretical insight into hydroxyl production via H₂O₂ decomposition over the Fe₃O₄ (311) surface. *RSC Adv* 11 (57), 36257–36264 doi 10.1039/D1RA06943H.
- [43] Ling, C., Liu, X., Li, H., Wang, X., Gu, H., Wei, K., Li, M., Shi, Y., Ben, H., Zhan, G., Liang, C., Shen, W., Li, Y., Zhao, J., Zhang, L., 2022. Atomic-Layered Cu₅ Nanoclusters on FeS₂ with Dual Catalytic Sites for Efficient and Selective H₂O₂ Activation. *Angew Chem* 134 (21), e202200670.
- [44] Lohr, L.L., 1972. Spin-forbidden electronic excitations in transition metal complexes. *Coord Chem Rev* 8, 241–259.
- [45] Martra, G., Chiardola, E., Coluccia, S., Marchese, L., Tomatis, M., Fubini, B., 1999. Reactive sites at the surface of crocidolite asbestos. *Langmuir* 15 (18), 5742–5752.
- [46] Moretti, G., Fierro, G., Ferraris, G., Andreozzi, G.B., Naticchioni, V., 2014. N₂O decomposition over [Fe]-MFI catalysts. *Influ Fe_xO_y Nucl Presence Framew Alum Catal Act J Catal* 318, 1–13 doi 10.1016/j.jcat.2014.07.005.
- [47] Muniz-Miranda, F., Menziani, M.C., Pedone, A., 2015. DFT and TD-DFT assessment of the structural and optoelectronic properties of an organic-ag14 nanocluster. *J Phys Chem A* 119 (21), 5088–5098 doi 10.1021/jp507679f.
- [48] Muniz-Miranda, F., Menziani, M.C., Pedone, A., 2016. Assessment of the basis set effect on the structural and electronic properties of organic-protected gold nanoclusters. *Theor Chem Acc* 135, 1–9. https://doi.org/10.1007/s00214-016-1856-2.
- [49] Nozaki, C., Lugmair, C.G., Bell, A.T., Tilley, T.D., 2002. Synthesis, characterization, and catalytic performance of single-site iron (III) centers on the surface of SBA-15 silica. *J Am Chem Soc* 124 (44), 13194–13203.
- [50] Pacella, A., Andreozzi, G.B., Ballirano, P., Gianfagna, A., 2008. Crystal chemical and structural characterization of fibrous tremolite from Ala di Stura (Lanzo Valley, Italy). *Per Min* 77 (2), 51–62.
- [51] Pacurari, M., Castranova, V., Vallyathan, V., 2010. Single-and multi-wall carbon nanotubes versus asbestos: are the carbon nanotubes a new health risk to humans? *J Toxicol Environ Health, Part A* 73 (5-6), 378–395.
- [52] Perdev, J.P., Ruzsinszky, A., Csonka, G.I., Vydrov, O.A., Scuseria, G.E., Constantin, L.A., Zhou, X., Burke, K., 2007. Restoring Density-gradient Expans *Exch Solids Surf* 100, 136406. https://doi.org/10.1103/PhysRevLett.100.136406.
- [53] Pérez-Ramírez, J., Groen, J.C., Brückner, A., Kumar, M.S., Bentrup, U., Debbagh, M.N., Villaescusa, L.A., 2005. Evolution of isomorphously substituted iron zeolites during activation: comparison of Fe-beta and Fe-ZSM-5. *J Catal* 232 (2), 318–334.
- [54] Pirngruber, G.D., Roy, P.K., Prins, R., 2006. On determining the nuclearity of iron sites in Fe-ZSM-5—a critical evaluation. *Phys Chem Chem Phys* 8 (34), 3939–3950.
- [55] Pollastri, S., Gualtieri, A.F., Gualtieri, M.L., Hanuskova, M., Cavallo, A., Gaudino, G., 2014. The zeta potential of mineral fibres. *J Haz Mat* 276 469–479.
- [56] Pollastri, S., D'Acapito, F., Trapananti, A., Colantoni, I., Andreozzi, G.B., Gualtieri, A.F., 2015. The chemical environment of iron in mineral fibres. A combined X-ray absorption and Mössbauer spectroscopic study. *J Haz Mat* 298, 282–293.
- [57] Pollastri, S., Gigli, L., Ferretti, P., Andreozzi, G.B., Gandolfi, N.B., Pollok, K., Gualtieri, A.F., 2017. The crystal structure of mineral fibres. 3. Actinolite asbestos. *Per Min* 86 (2), 89–98.
- [58] Pollastri, S., Gigli, L., Ferretti, P., Andreozzi, G.B., Bursi Gandolfi, N., Pollok, K., Gualtieri, A.F., 2017. The crystal structure of mineral fibres: 3. Actinolite Asbestos. *Per Min* 86, 89–98.
- [59] Pollastri, S., Perchiazzi, N., Lezzerini, M., Plaisier, J.R., Cavallo, A., Dalconi, M.C., Bursi Gandolfi, N., Gualtieri, A.F., 2016. The crystal structure of mineral fibres: 1. Chrysotile. *Per Min* 85, 249–259.
- [60] Pollastri, S., Perchiazzi, N., Gigli, L., Ferretti, P., Cavallo, A., Bursi Gandolfi, N., Pollok, K., Gualtieri, A.F., 2017. The crystal structure of mineral fibres: 2. Amosite and fibrous antophyllite. *Per Min* 86, 55–65.
- [61] Schwidder, M., Kumar, M.S., Klementiev, K., Pohl, M.M., Brückner, A., Grünert, W., 2005. Selective reduction of NO with Fe-ZSM-5 catalysts of low Fe content: I. Relations between active site structure and catalytic performance. *J Catal* 231 (2), 314–330.
- [62] Segall, M.D., Lindan, P.J.D., Probert, M.J., Pickard, C.J., Hasnip, P.J., Clark, S.J., Payne, M.C., 2002. First-principles simulation: ideas, illustrations and the CASTEP code. *J Phys -Condens Matter* 14, 2717–2744. https://doi.org/10.1088/0953-8984/14/11/301.
- [63] Sherman, D.M., Waite, T.D., 1985. Electronic spectra of Fe³⁺ oxides and oxide hydroxides in the near IR to near UV. *Am Min* 70 (11-12), 1262–1269.
- [64] Stoch, P., Stoch, A., Ciecinska, M., Krakowiak, I., Sitarz, M., 2016. Structure of phosphate and iron-phosphate glasses by DFT calculations and FTIR/Raman spectroscopy. *J Non-Cryst Solids* 450, 48–60.
- [65] Sun, Y., Zhou, P., Zhang, P., Meng, S., Zhou, C., Liu, Y., Zhang, H., Xiong, Z., Duan, X., Lai, B., 2022. New insight into carbon materials enhanced Fenton oxidation: A strategy for green iron (III)/iron (II) cycles. *Chem Eng J* 450, 138423.
- [66] Toyokuni, S., 2009. Role of iron in carcinogenesis: cancer as a ferrotoxic disease. *Cancer Sci* 100 (1), 9–16.
- [67] Wadt, W.R., Hay, P.J., 1985. *Ab initio* effective core potentials for molecular calculations - 10-potentials for main group elements Na to Bi. *J Chem Phys* 82, 284–298 doi 10.1063/1.448800.
- [68] Windig, W., Stephenson, D.A., 1992. Self-modeling mixture analysis of second-derivative near-infrared spectral data using the SIMPLISMA approach. *Anal Chem* 64 (22), 2735–2742.
- [69] Zecchina, A., Rivallan, M., Berlier, G., Lamberti, C., Ricchiardi, G., 2007. Structure and nuclearity of active sites in Fe-zeolites: comparison with iron sites in enzymes and homogeneous catalysts. *Phys Chem Chem Phys* 9, 3483–3499.